

A Simple and Rapid Method to Directly Synthesize TiO₂/SBA-16 with Different TiO₂ Loading and its Photocatalytic Degradation Performance on Rhodamine B

Jing Ma · Liangsheng Qiang · Xiangbo Tang · Hanyang Li

Received: 31 March 2010 / Accepted: 11 May 2010 / Published online: 25 May 2010
© Springer Science+Business Media, LLC 2010

Abstract SBA-16-supported TiO₂ photocatalysts was synthesized by internal hydrolysis method. The synthesized samples were characterized in detail by X-ray diffraction (XRD), Raman spectra, N₂ adsorption–desorption, transmission electron microscopy (TEM), UV–Visible absorption spectra and X-ray photoelectron spectroscopy (XPS). The results indicated that SBA-16 retained the 3D caged-like mesostructure while TiO₂ located almost inside the mesoporous channels in form of small crystals with anatase structure. The photodecomposition of Rhodamine B (RhB) in aqueous medium was selected to evaluate the photocatalysis performance of TiO₂/SBA-16. The influences of different TiO₂ loading were studied. The results indicated that TiO₂/SBA-16 synthesized by IH method showed much higher photodegradation ability towards RhB than pure TiO₂ and TiO₂/SBA-15.

Keywords TiO₂/SBA-16 · TiO₂ particles · Internal hydrolysis · Location · Photodegradation

1 Introduction

Metal oxide semiconductors, such as TiO₂, ZnO, ZnS and SnO₂, have shown a high efficiency in removal of highly toxic and non-biodegradable pollutants commonly present in air, domestic or industrial wastewater [1–3]. TiO₂ is regarded as the most promising one for its high photocatalytic activity, chemical/photocrossion stability, low cost and environmental-friendly [4]. However, in practical

applications, the TiO₂ particles tend to agglomerate into large particles resulting in a reduction of photocatalytic activity. Moreover, TiO₂ should be small enough to offer a high number of active sites. To overcome these drawbacks, it is advantageous to generate mesoporous titania [5] and mesoporous silica with incorporated TiO₂ [6]. The incorporation of TiO₂ within an ordered silica host with high surface area increases the active surface area of TiO₂ and catalytic activity [7–9].

Well-ordered mesoporous silica materials M41S [10] has been widely used for many purpose such as adsorption separation and catalysis for many years [11, 12]. SBA-16 is a type of highly interconnected 3-D mesoporous material with cubic *Im3m* structure, by using F127 as a structure-directing agent. Such type of highly interconnected 3D mesostructured porous material is expected to be superior to hexagonal structures with its unique 3D channel network which allows the guest species access the opened porous host easily [13]. However, unlike hexagonal SBA-15, little work has been carried out on metal incorporated SBA-16. This is probably due to difficulties encountered in the synthesis conditions as many factors such as acidity, temperature and molar ratio of the reactants have been involved.

Generally, synthesis of TiO₂/SBA-16 includes several steps, the most important of which is the incorporation of TiO₂ into the pore channels. The synthesis is done at acidic conditions which almost make all metal salts soluble and lost during the filtration process. So a very small amount of TiO₂ can be incorporated into the framework of SBA-16 and few researches about the properties and performance of TiO₂/SBA-16 were reported. Thus, it requires new appropriate synthesis approach which can provide an effective way to control the uniformity of TiO₂ particle size and induce controlled TiO₂ particle growth. And it is still a

J. Ma · L. Qiang (✉) · X. Tang · H. Li
Department of Chemistry, Harbin Institute of Technology,
Harbin 150001, China
e-mail: qianglshit@yahoo.com.cn

challenge to synthesize TiO₂ incorporated SBA-16 through a direct, simple, economical and efficient process.

In the present work, the structural and the photocatalytic properties of TiO₂/SBA-16 obtained by internal hydrolysis method were investigated. The texture, structure, and crystallization were investigated by X-ray diffraction (XRD), Raman spectra, N₂ adsorption–desorption, transmission electron microscopy (TEM), UV–Visible absorption spectra and X-ray photoelectron spectroscopy (XPS). The photo-decomposition of Rhodamine B (RhB) in aqueous medium was selected to evaluate the photocatalysis performance of TiO₂/SBA-16 and compare with commercial pure TiO₂ and TiO₂/SBA-15. This work may provide new insights into the preparation of photocatalysts.

2 Experimental

2.1 Catalyst Preparations

SBA-16 was prepared according to the previously reported procedure [14–16] by reaction from a solution of tri-block copolymer F127 (EO₁₀₆PO₇₀EO₁₀₆, Aldrich) and tetraethoxysilane (TEOS). Typically, 5 g of the F127 polymer were dissolved in 240 mL of 0.5 M HCl and stirred for 4 h at 38 °C. After complete dissolution, desired amount of *n*-butanol (BuOH) and TEOS were added to the solution and then stirred vigorously for 24 h. The molar composition was varied in the range of (0.0035F127/*x*TEOS/*y*BuOH/0.91HCl/117H₂O) with *x* = 0.9–2.2 and *y* = 0.76–2.08. The resulting mixture was kept at 100 °C in an oven for 24 h. The resulting white solid was separated by filtration, washed with de-ionized water, dried under vacuum for 24 h and calcined in air at 550 °C for 6 h.

TiO₂ was incorporated into SBA-16 by internal hydrolysis (IH) method which different from the procedure of Roie Zukerman [17]. Tetrabutyl titanate (TBT) was used as titanium source instead of titanium isopropoxide (TTIP). The preparation process of TiO₂/SBA-16 was as follows (Fig. 1). In order to get different Si:Ti ratio, different amount of TBT (range from 0.46 to 7.36 mL) in ethanol solution (the volume ratio of ethanol to TBT is 5) was prepared. 0.5 g of SBA-16 was added to the above solution

and stirred for 1 h to make TBT adsorb on the surface and channels of SBA-16. Next, desired amount of H₂O was added to the solution and stirred for 2 h to hydrolyze TBT completely. Finally, the as-synthesized samples were separated by filtration, washed with anhydrous ethanol, dried at 80 °C overnight and calcined at 550 °C for 3 h. The operation of washing with ethanol is essential to remove unanchored titanium species from the surface of SBA-16. The samples are designated as TiO₂/SBA-16(*x*), TiO₂ loading for all samples are reported in Table 1, where *x* means the amount of TBT in the initial mixture.

2.2 Characterization Techniques

Low-angle and wide-angle XRD patterns were performed between 0.6°–5° and 10°–80° (2θ), respectively, on a Siemens D5005 instrument with Cu Kα (λ = 0.154 nm) radiation. Raman spectra were measured with JOBIN YVON HR800 Raman spectrophotometer (France) in the range of 100–1600 cm^{−1}, using an Ar ion laser beam and an excitation wave length of 457.9 nm. The spectra were recorded at room temperature by the condition of 50 s integral time at a 1 cm^{−1} resolution. N₂ adsorption/desorption isotherms were measured at 77 K in a Quantachrome Autosorb-1 sorption analyzer. Samples were outgassed at 300 °C for 10 h before the measurement. The Brunauer–Emmett–Teller (BET) method was used to calculate the surface area. The pore size distributions were calculated with the DFT Plus software (Micromeritics), applying the Barrett–Joyner–Halenda (BJH) model with cylindrical geometry of the pores. TEM and HRTEM were performed by a FEI Tecnai G2 S-Twin electron microscope with an acceleration voltage of 200 kV. Prior to the analysis the samples were dispersed in acetone, stirred in an ultrasonic bath and placed on a carbon-coated copper grid. UV–Visible absorption spectra scans were performed on a Shimadzu UV-2550 spectrometer in the range from 250 to 600 nm with a resolution of 1 nm. BaSO₄ was used as a reflectance standard material during the experiment. XPS was obtained using a physical electronics model PHI5700 X-ray photoelectron spectrometer with Mg Kα X-rays. The binding energies were calibrated with reference to C1s at 285 eV.

Fig. 1 Schematic representation of the synthesis route for TiO₂/SBA-16

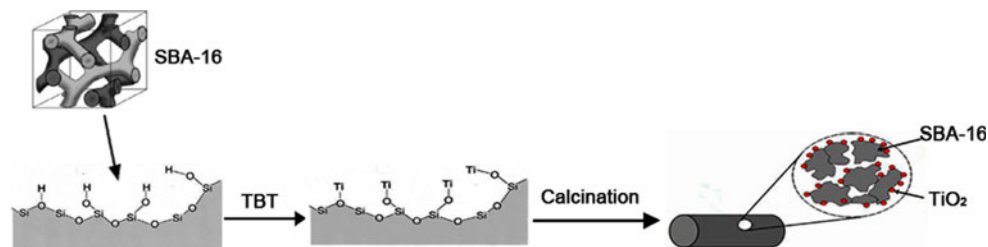


Table 1 Textural properties and average TiO₂ crystal size of SBA-16 and TiO₂/SBA-16(*x*)

Sample	Si:Ti ratio ^a	<i>a</i> ₀ (nm)	BET area (m ² /g)	<i>V</i> _{tot} ^b (cm ³ /g)	Average pore diameter (nm)	Average TiO ₂ crystal size (nm)
SBA-16	∞	13.88	941.8	0.704	5.236	0
TiO ₂ /SBA-16(0.46)	74.0	13.61	593.3	0.642	4.953	2.242
TiO ₂ /SBA-16(0.92)	57.2	13.56	467.2	0.518	4.324	2.887
TiO ₂ /SBA-16(1.84)	34.8	13.52	522.3	0.492	4.149	3.051
TiO ₂ /SBA-16(3.68)	28.6	13.48	421.9	0.355	4.083	3.516
TiO ₂ /SBA-16(7.36)	12.7	13.23	414.8	0.304	4.077	4.054

^a TiO₂ loading was measured by ICP

^b *V*_{tot} was the total pore volume

2.3 Adsorption and Photocatalytic Test

For all samples, the adsorption and photocatalytic activity were investigated. The photocatalytic activity was tested by photodegradation of RhB in aqueous solution in a photolysis glass reactor. The UV-source was a 125 W medium pressure Hg lamp (365 nm, from Tianjin Lvhuan Unique Lamp Company) with a double wall jacket in which water was circulated to prevent overheating of the reaction mixture. The UV-light irradiated perpendicularly to the surface of the suspension and the distance from the UV source to the suspension was 10 cm. TiO₂/SBA-16(*x*) (5 mg) was added to a suspension of RhB (100 mL, 1×10^{-5} M) and stirred for 30 min without UV irradiation at room temperature in order to establish an adsorption/desorption equilibrium between RhB and the surface of the catalyst. Next, the solution was illuminated for 90 min with UV-light. During this illumination, the suspension (5 mL) was collected at fixed intervals (15 min) and analyzed by ultraviolet spectrophotometer (722 N from Shanghai Fine Instrument Company). The absorbance was measured at 553 nm with water as reference and converted to concentration with Lambert–Beer’s law. (Lambert–Beer’s Law, $A = \varepsilon bC$, where A absorption, ε proportion constant, b light length, C concentration).

3 Results and Discussions

3.1 Textural Properties and Characterization

The low-angle XRD patterns of SBA-16 and TiO₂/SBA-16(*x*) are shown in Fig. 2a. SBA-16 possess three reflections: (110), (200), (211) with *d*-value, which are consistent with a cubic *Im3m* symmetry. All of the TiO₂/SBA-16(*x*) samples display similar XRD patterns to the parent SBA-16, indicating they are still SBA-16-type. However, the diffraction intensity of the (100) reflection gradually decreased with increasing TiO₂ loading leads to reduces

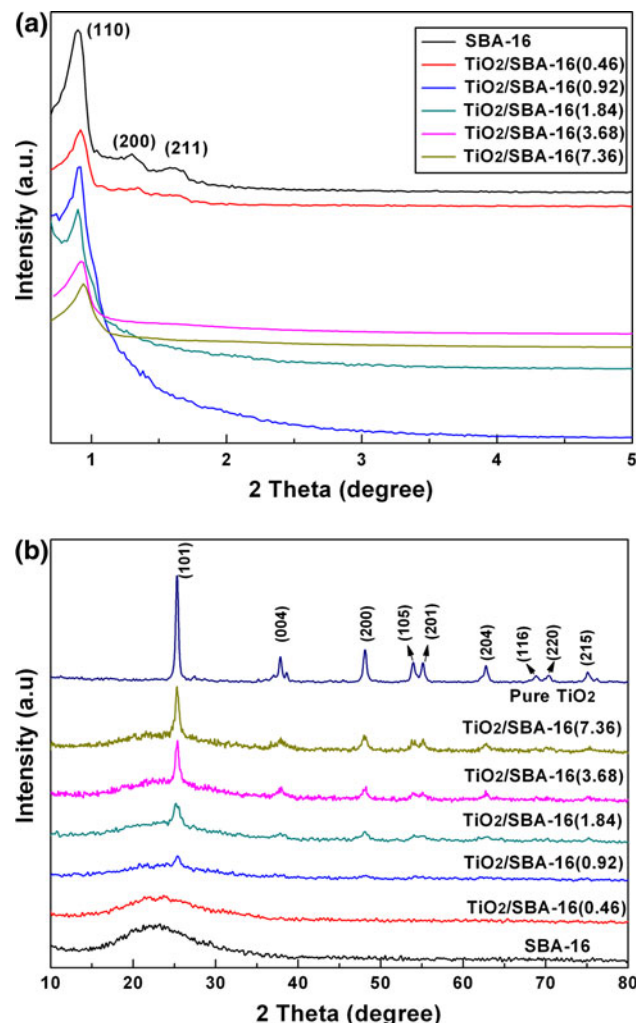


Fig. 2 XRD analysis of SBA-16 and TiO₂/SBA-16(*x*). **a** Low-angle XRD, **b** wide-angle XRD

the order of the mesostructures. Furthermore, it can also be seen that the position of the (100) diffraction peak shifted to a higher angle, suggesting that the pore size of the samples became smaller, which is due to the fact that the

TiO₂ particles exhibits inside the mesopores of the SBA-16 structure [18].

Figure 2b shows the wide angle XRD pattern of SBA-16 and TiO₂/SBA-16(x). A typical characteristic amorphous broad peak centered at 22° of 2θ is observed for SBA-16. The XRD patterns of TiO₂ shows nine peaks at 25.3°, 37.8°, 48.1°, 54.6°, 55.0°, 62.6°, 68.9°, 70.3° and 75.1°, that can be indexed to the crystal planes of anatase. The intensity of the TiO₂/SBA-16 reflections increased with the increase loading of TiO₂. These results indicate that a part of TiO₂ particles disperse into the pore of SBA-16. In the case of TiO₂/SBA-16(0.46), it shows only a broad peak corresponding to the reflection plane (101) of anatase. This indicated that the TiO₂ is mainly in the amorphous form with a small amount of anatase phase. The peaks of the TiO₂/SBA-16 are much smaller and broader at half-maximum height compared to TiO₂. This indicates that the TiO₂ particles are small in size when deposited on SBA-16. The size of TiO₂ in the mesostructure of SBA-16 is under 5 nm compared with 22.7 nm for the pure TiO₂ (shown in Table 1), which was calculated according to the Scherrer diffraction formula ($D = \kappa\lambda/\beta\cos\theta$). This indicated that the limited pore channels of SBA-16 restrict the growth of TiO₂ particles by IH method.

Raman spectra are known as a sensitive tool for detection of anatase crystal even at very low loading [19]. Figure 3 shows the Raman spectra of TiO₂/SBA-16(x). Bands at 147, 398, 520 and 641 cm⁻¹ generated by the present of TiO₂ prove the real existence of anatase phase [20]. With low amounts of TiO₂ loading (the TBT amount is 0.46 mL), only one faint band at about 147 cm⁻¹, assigned to the Eg(1) peak, was observed. The intensity of the Eg(1) peak increases with the TiO₂ loading increased. As the TBT amount is above 1.84 mL, three un conspicuous peaks at 398, 520, and 641 cm⁻¹ appear as could be

expected from the relative high TiO₂ loading. The intensity of the anatase bands of the sample TiO₂/SBA-16(3.68) and TiO₂/SBA-16(7.36) remains unchanged but higher than the relative intensity of sample TiO₂/SBA-16(1.84), indicating a higher amount of anatase phase in the SBA-16.

The adsorption–desorption isotherms for SBA-16 and TiO₂/SBA-16 are shown in Fig. 4 (TiO₂/SBA-16(0.92) and TiO₂/SBA-16(3.68) are not shown). The samples exhibit isotherms of typical type IV with a H₂ hysteresis loop due to the capillary condensation steps at relative pressure of $0.4 < p/p_0 < 0.8$, which suggest the presence of 3D caged-like mesopores [21, 22]. It can be clearly observed that the amount of N₂ adsorption decreases and the inflection point in the isotherm of TiO₂/SBA-16 shows a shift to a smaller relative pressure, indicating that the mesostructure is maintained upon TiO₂ addition and the present TiO₂ leads to a marked change in the shape of the hysteresis loop. Such a significant change of N₂ adsorption for TiO₂/SBA-16 is reasonable, considering the formation of TiO₂ particles inside the mesopores of SBA-16. Furthermore, the decrease in N₂-sorption confirms the decrease of the interparticle pores in size. The textural properties and average TiO₂ size for these materials were summarized in Table 1. When the TiO₂ loading is low, the TiO₂ particles are located inside the mesopores of SBA-16. It seems that the mesoporous channels of SBA-16 controlled the size of TiO₂ particles in a certain extent. If the TiO₂ loading is high, TiO₂ particles are located inside closing the pore or outside the pores [19]. Therefore, larger TiO₂ clusters will obstruct the pores of the SBA-16, resulting in low pore volumes. This trend is in good agreement with previous observations about TiO₂/SBA-15 [23–27].

The TEM images of TiO₂/SBA-16(x) are shown in Fig. 5. The image clearly showed the well-ordered body-centered mesostructure and with the *Im3m* space group

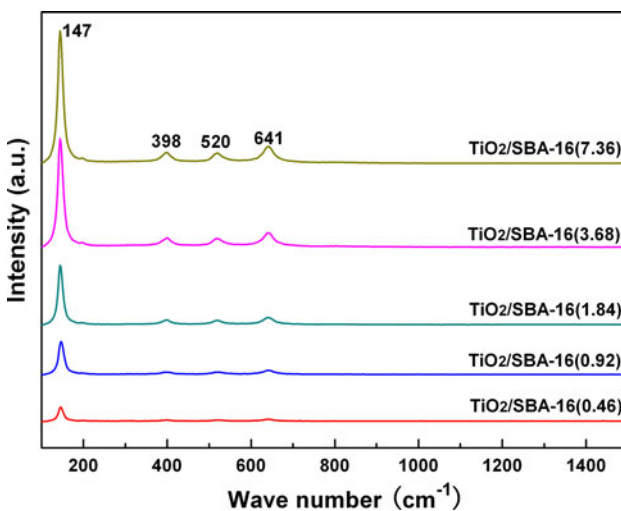


Fig. 3 Raman spectra of TiO₂/SBA-16(x)

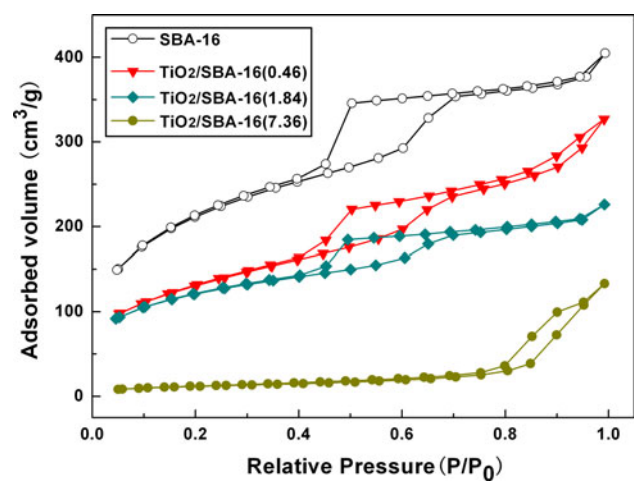


Fig. 4 N₂ adsorption–desorption isotherms of SBA-16 and TiO₂/SBA-16(x)

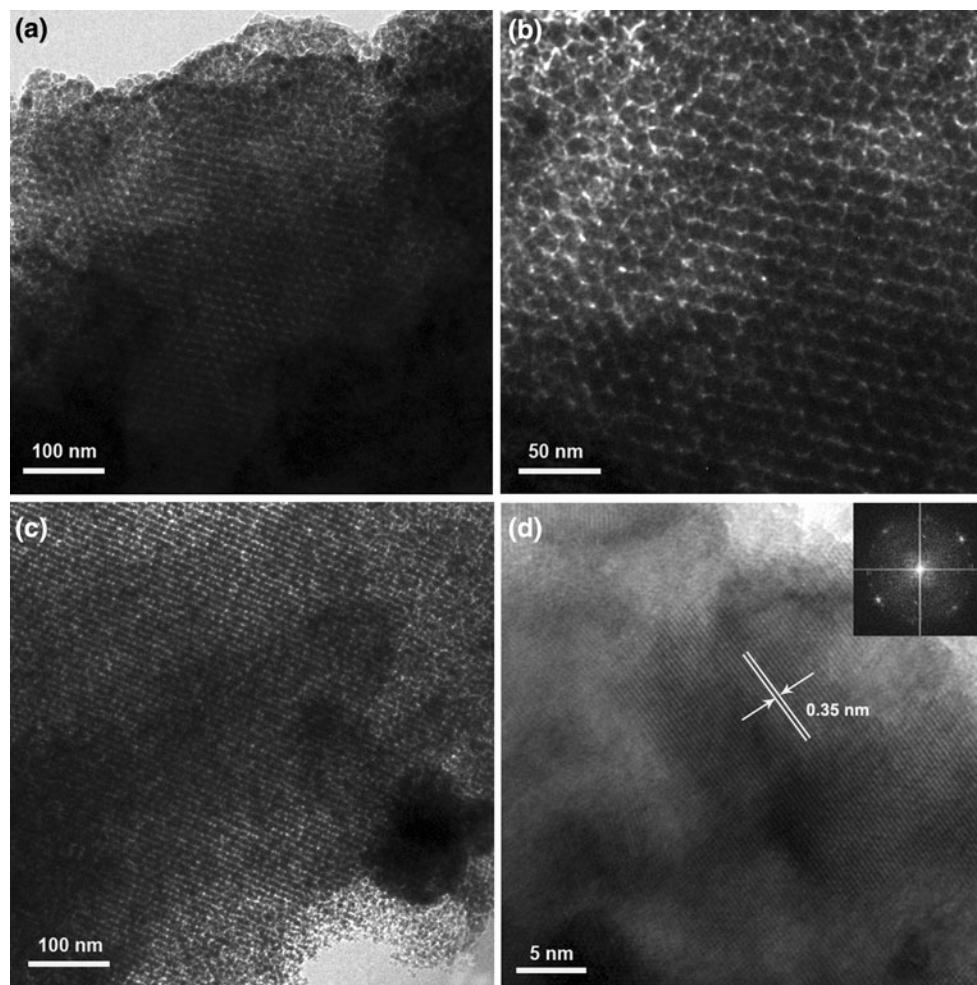


Fig. 5 TEM micrographs of $\text{TiO}_2/\text{SBA-16}(x)$. **a** $\text{TiO}_2/\text{SBA-16}(0.92)$, **b** $\text{TiO}_2/\text{SBA-16}(1.84)$, **c** $\text{TiO}_2/\text{SBA-16}(3.68)$, **d** HRTEM image of the TiO_2 (the corresponding FFT pattern is *inset*)

(as shown in Fig. 5a, b, c). The results indicated that the IH method could not destroy the framework of SBA-16, although there is a decrease of the order of SBA-16. It is the direct evidence of the formation of TiO_2 particles inside the pore channels of SBA-16. The pore diameter estimated from the TEM micrograph is ca. 5.2 nm. For $\text{TiO}_2/\text{SBA-16}(3.68)$, TiO_2 particles (appeared as dark substances) are located inside the mesopore channels of the SBA-16. However, larger TiO_2 particles can also be found in the TEM observations, which indicated that there are TiO_2 particles existed outside the pore channels of the SBA-16 (Fig. 5c). The lattice fringes can be easily observed from the HRTEM image. The measured lattice distance of 0.35 nm is a good agreement with (101) lattice distance of anatase TiO_2 . The result is consistent with the Fourier diffractogram shown in the inset of Fig. 5d. The results suggested that TiO_2 could successfully grow inside the pore channels of the host SBA-16 and also could locate outside the pores in spite of the high TiO_2 loading.

Figure 6 shows the UV–Visible absorption spectra for $\text{TiO}_2/\text{SBA-16}$ and pure TiO_2 . Pure TiO_2 only shows absorption less than 400 nm due to the intrinsic band gap absorption. The absorption band edges of $\text{TiO}_2/\text{SBA-16}(x)$ shifts towards shorter wavelength in compare with pure TiO_2 , due to the quantum effect of the semiconductor compound [27, 28]. This phenomenon indicates the increasing of the forbidden band energy. Since the particle size of the semiconductor compound is inversely proportional to the forbidden band energy, the blue shift of the absorption edge apparently indicates the smaller TiO_2 particle size limited by SBA-16 channels.

Figure 7 show O (1s) XPS spectra of $\text{TiO}_2/\text{SBA-16}(0.92)$. It reveals three O 1s peaks at 527.23, 528.9 and 531.15 eV. Two peaks at binding energies of 531.15 and 527.23 eV are assigned to oxygen in Si–O–Si and Ti–O–Ti bonds, respectively [29]. Furthermore, a peak at an intermediate binding energy value of 528.9 eV was attributed to the hydroxyl groups or chemisorbed water molecules

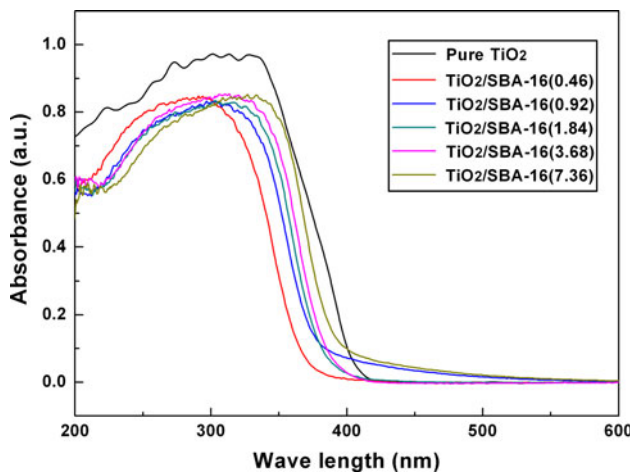


Fig. 6 O (1s) XPS spectra analysis of TiO₂/SBA-16(0.92)

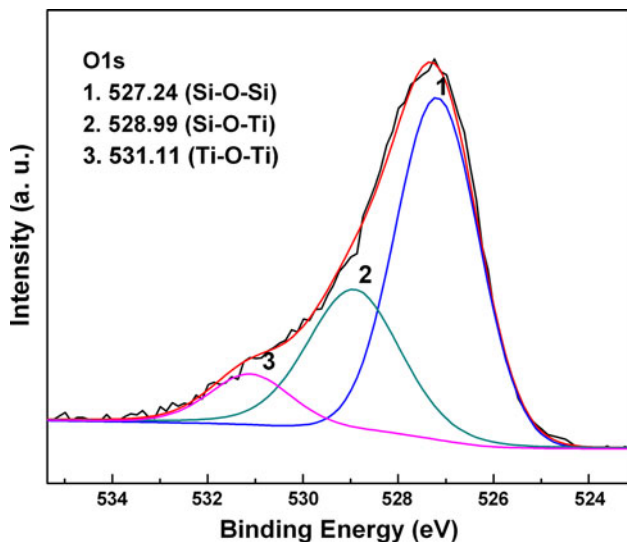


Fig. 7 UV-Visible absorption spectra of TiO₂/SBA-16(x)

adsorbed on TiO₂ surface, which is produced by the oxygen in interfacial Si–O–Ti cross-linking bonds [30]. It is noted that O 1s spectra have a small binding energy shift compared with that of pure TiO₂ in the reported literatures [31–33]. This may be ascribed to an increase in the ionic state of the oxygen bond when TiO₂ incorporate into SBA-16.

3.2 The Adsorption and Photocatalytic Activity of TiO₂/SBA-16

For all samples, the adsorption and photocatalytic activity were investigated. The photocatalytic activity of the TiO₂/SBA-16(x) samples was evaluated for RhB under UV irradiation and the activity was also compared with TiO₂/SBA-15(0.92) and pure TiO₂ samples. There was no RhB photodegradation without any catalyst and irradiation

in the preliminary test. It is believed that the decrease of the RhB concentration over the photocatalyst depends on two factors: the adsorption and the photodegradation of the RhB. In the absence of UV irradiation, the concentration of RhB rapidly decreases for all the samples. The adsorption capacity of TiO₂/SBA-16 was measured during 60 min. For the low amount of TiO₂ loadings, it takes 30 min before the adsorption–desorption equilibrium is reached and the samples exhibits higher adsorption capability due to its highest specific surface area and pore volume (59.34% RhB). When the TiO₂ loading is high, it takes 20 min to reach adsorption–desorption equilibrium, which is difficult for the RhB to pass the narrowed pores and approach the TiO₂ particles inside the SBA-16 channels [19]. The addition of TiO₂ added has a strong effect on the mesoporous structure and was found to strongly influence the adsorption capacity and photocatalytic activity. Therefore, the RhB adsorbed on the samples decreased with an increasing amount of titania, due to the decrease in specific surface area, pore volume and pore radius (Fig. 8).

The photodegradation of RhB in the presence of TiO₂/SBA-16(x) is shown in Fig. 9. We observed the significantly photodegradation activity for the TiO₂/SBA-16. The activities decrease in the following order: TiO₂/SBA-16(0.92) > TiO₂/SBA-16(3.68) > TiO₂/SBA-16(1.84) > TiO₂/SBA-16(0.46) > TiO₂/SBA-16(7.36) > TiO₂/SBA-15(0.92) > pure TiO₂.

It is known that photodegradation kinetics follow Langmuir–Hinshelwood kinetics model [34, 35]. The reaction can be represented as follows (Eq. 1):

$$R = -\frac{dC}{dt} = \frac{k_r KC}{1 + KC} \quad (1)$$

where k_r is the reaction rate constant, K is the adsorption coefficient of the RhB at the surface of SBA-16 and C is the concentration of the RhB solution. When C is very

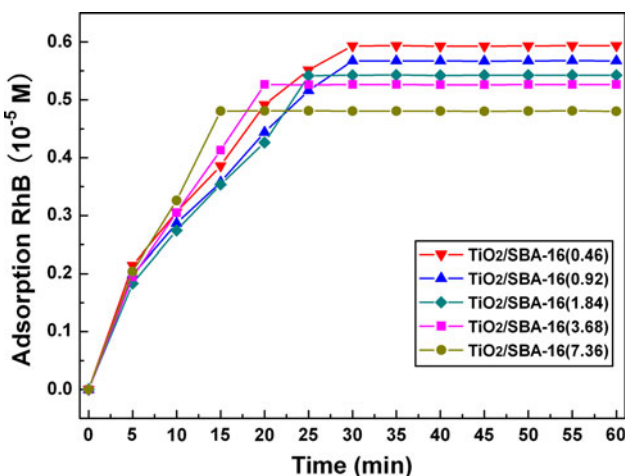


Fig. 8 Adsorption of RhB on TiO₂/SBA-16(x)

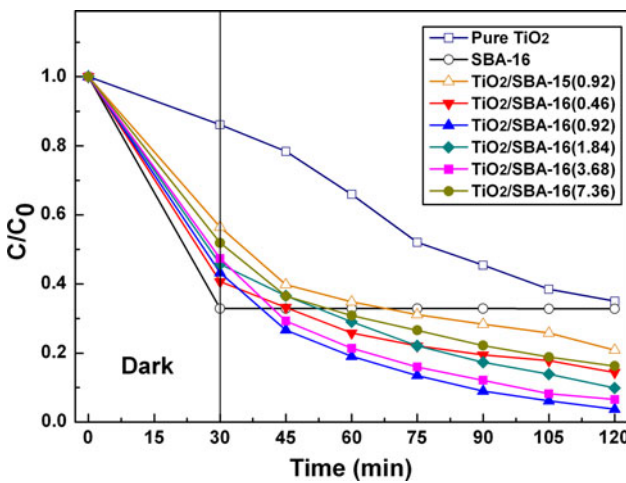


Fig. 9 The degradation curves of RhB by the $\text{TiO}_2/\text{SBA-16}(x)$

small, the KC product is negligible with respect to unity so that Eq. 1 describes first-order kinetics. The integration of Eq. 1 with the limit condition that at the start of irradiation, $t = 0$, the concentration is the initial one, $C = C_0$, giving Eq. 2:

$$\ln \frac{C_0}{C} = k_{\text{app}} t = k_r K t \quad (2)$$

where k_{app} is the apparent first-order reaction constant, C_0 is the initial concentration of the RhB solution. A kinetic linear simulation curve of RhB photocatalytic degradation using $\text{TiO}_2/\text{SBA-16}(x)$ is shown in Fig. 10. The fact that the curve showed good linearity indicating that the photocatalytic degradation of RhB using $\text{TiO}_2/\text{SBA-16}$ as catalyst fits well with the first-order reaction kinetics. The values of k_{app} for $\text{TiO}_2/\text{SBA-16}$ are calculated and listed in Table 2. k_{app} value of the catalyst $\text{TiO}_2/\text{SBA-16}(0.92)$ is

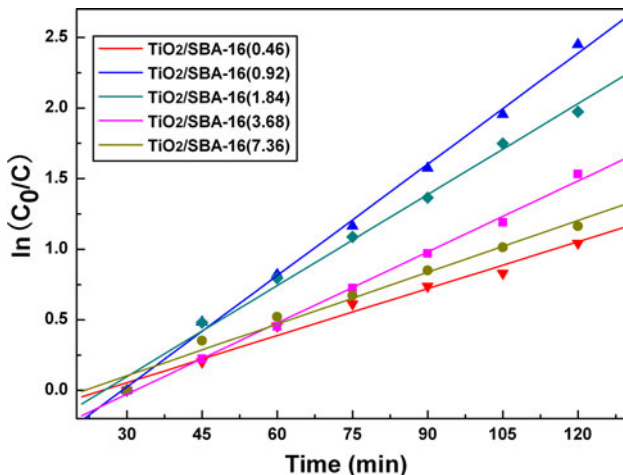


Fig. 10 Kinetic linear simulation curve of RhB photocatalytic degradation by $\text{TiO}_2/\text{SBA-16}(x)$

Table 2 The rate constant of $\text{TiO}_2/\text{SBA-16}(x)$ for RhB photodegradation

Sample	k_{app} (min^{-1})
Pure TiO_2	0.0102
$\text{TiO}_2/\text{SBA-15}(0.92)$	0.0122
$\text{TiO}_2/\text{SBA-16}(0.46)$	0.0147
$\text{TiO}_2/\text{SBA-16}(0.92)$	0.0272
$\text{TiO}_2/\text{SBA-16}(1.84)$	0.0172
$\text{TiO}_2/\text{SBA-16}(3.68)$	0.0226
$\text{TiO}_2/\text{SBA-16}(7.36)$	0.0134

0.0272 min^{-1} , which is much higher than that of pure TiO_2 and $\text{TiO}_2/\text{SBA-15}(0.92)$ (0.0102 and 0.0122 min^{-1} , respectively). However, $\text{TiO}_2/\text{SBA-16}(7.36)$ has the rate constant of 0.0134 min^{-1} .

Among all of the photocatalysts, $\text{TiO}_2/\text{SBA-16}(0.92)$ exhibits the most excellent photocatalytic activity, whereas $\text{TiO}_2/\text{SBA-16}(0.46)$ shows lower activity even if it has the highest adsorption ability. This can be due to the different position of the TiO_2 particles, which affects the photocatalytic activity.

When the TiO_2 loading is low, the particles can be located inside the channels. But when the TiO_2 loading is further increased, the large amount of TiO_2 on the external surface cannot approach to the RhB molecules, leading to a decreased photocatalytic activity. This lower photocatalytic activity indicated that the accessibility of the anatase nanoparticles has decreased in a large extent. The large amount of particles on the external surface leads to a bad accessibility of all nanoparticles [19]. In case of $\text{TiO}_2/\text{SBA-16}(7.36)$ with the highest TiO_2 loading, the lower adsorption capacity and photocatalytic activity may result from the extra amount of TiO_2 present in the sample, causing difficulty in passing to the RhB. These results indicate that both the adsorption capability of SBA-16 and influence of the photocatalytic activity from the amount of the TiO_2 . Thus, an optimal amount of TiO_2 loading is crucial for the photocatalyst. When the loading is too high, TiO_2 particles will gather into larger particles and block the mesopores of SBA-16, leading to decrease of photocatalytic activity. Moreover, it can be explained by the quantum size effect [20]. On the contrary, if the loading is too small, the photoactive sites are relatively low, which leads to the increase of average distance from the photoactive sites to the adsorption sites. In conclusion, $\text{TiO}_2/\text{SBA-16}(0.92)$ shows efficient photocatalytic degradation towards RhB among the $\text{TiO}_2/\text{SBA-16}$ samples. Moreover, it is conclude that 3D mesostructures and long range ordered structures [36] can promote effective degradation of RhB by enhancing the diffusion of reactants to the reactive sites of TiO_2 [37].

4 Conclusions

TiO₂/SBA-16 with different TiO₂ loading was prepared using IH method. The TiO₂/SBA-16(0.92) shows efficient photocatalytic activity towards RhB degradation than pure TiO₂ and TiO₂/SBA-15(0.92) under UV irradiation. The high specific surface area and pore volume for TiO₂/SBA-16 with 3D mesostructure were prone to have high adsorption capability and easier diffusion to the photo-oxidative towards RhB. TiO₂ dispersed in mesostructure in form of small crystals with anatase structure and its size was limited by the channel of SBA-16, which could provide more photo-oxidative sites due to quantum effect, leading to improvement of its photocatalytic activity.

References

1. Hoffmann MR, Martin ST, Choi WY, Bahnemann DW (1995) Chem Rev 95:69
2. López-Muñoz M-J, Grieken RV, Aguado J, Marugán J (2005) Catal Today 101:307
3. Halasi Gy, Kecskeméti A, Solymosi F (2010) Catal Lett 135:16
4. Han P, Wang XM, Qiu XP, Ji XL, Gao LX (2007) J Mol Catal A Chem 272:136
5. Somorjai GA, Tao F, Park JY (2008) Top Catal 47:1
6. Li G, Zhao XS (2006) Ind Eng Chem Res 45:3569
7. Witte KDe, Busuioc AM, Meynen V, Mertens M, Bilba N, Van Tendeloo G, Cool P, Vansant EF (2008) Microporous Mesoporous Mater 110:100
8. Yue WB, Xu XX, Irvine JTS, Attidekou PS, Liu C, He HY, Zhao DY, Zhou WZ (2009) Chem Mater 21:2540
9. Busuioc AM, Meynen V, Beyers E, Cool P, Bilba N, Vansant EF (2007) Catal Commun 8:527
10. Kresge CT, Leonowicz ME, Roth WJ, Vartuli JC, Beck JS (1992) Nature 359:710
11. Lestari S, Mäki-Arvela P, Eränen K, Beltramini J, Max Lu GQ, Yu D, Murzin (2010) Catal Lett 134:250
12. Yang J, Zhang J, Zhu LW, Chen SY, Zhang YM, Tang Y, Zhu YL, Li YW (2006) J Hazard Mater 137:952
13. Gallo JMR, Bisio C, Marchese L, Pastore HO (2008) Microporous Mesoporous Mater 111:632
14. Zhao D, Feng J, Huo Q, Melosh N, Fredrickson GH, Chmelka BF, Stucky GD (1998) Science 279:548
15. Yang PD, Zhao DY, Margolese DI, Chmelka BF, Stucky GD (1998) Nature 396:152
16. Jin ZW, Wang XD, Cui XG (2007) J Colloid Interface Sci 307:158
17. Zukerman R, Vradman L, Titelman L, Weidenthaler C, Landau MV, Herskowitz M (2008) Microporous Mesoporous Mater 116:237
18. Yang CM, Liu PH, Ho YF, Chiu CY, Chao KJ (2003) Chem Mater 15:275
19. Beyers E, Biemans E, Ribbens S, Witte KDe, Mertens M, Meynen V, Bals S, Van Tendeloo G, Vansant EF, Cool P (2009) Appl Catal B Environ 88:515
20. Busuioc AM, Meynen V, Beyers E, Mertens M, Cool P, Bilba N, Vansant EF (2006) Appl Catal A Gen 312:153
21. Huo QS, Leon R, Petroff PM, Stucky GD (1995) Science 268:1324
22. Stevens WJJ, Lebeau K, Mertens M, Van Tendeloo G, Cool P, Vansant EF (2006) J Phys Chem B 110:9183
23. Landau MV, Vradman L, Wang X, Titelman L (2005) Microporous Mesoporous Mater 78:117
24. Sun DH, Liu ZM, He J, Han BX, Zhang JL, Huang Y (2005) Microporous Mesoporous Mater 80:165
25. Chiker F, Nogier JP, Launay F, Bonardet JL (2003) Appl Catal A Gen 243:309
26. Yang HC, Lin HY, Chien YS, Wu JCS, Wu HH (2009) Catal Lett 131:381
27. Perathoner S, Lanzafame P, Passalacqua R, Centi G, Schlägl R, Su DS (2006) Microporous Mesoporous Mater 90:347
28. Morey MS, O'Brien S, Schwarz S, Stucky GD (2000) Chem Mater 12:898
29. Kang M, Lee MH (2005) Appl Catal A Gen 284:215
30. Hung WC, Chen YC, Chu H, Tseng TK (2008) Appl Surf Sci 255:2205
31. Sahu DR, Hong LY, Wang SC, Huang JL (2009) Microporous Mesoporous Mater 117:640
32. Ren WJ, Ai ZH, Jia FL, Zhang LZ, Fan XX, Zou ZG (2007) Appl Catal B Environ 69:138
33. Bian ZF, Zhu J, Wang SH, Cao Y, Qian XF, Li HX (2008) J Phys Chem C 112:6258
34. Li YZ, Kim SJ (2005) J Phys Chem B 109:12309
35. Zheng S, Cai Y, O'Shea KE (2010) J Photochem Photobiol A Chem 210:61
36. Grudzien RM, Pikus S, Jaroniec M (2006) J Phys Chem B 110:2972
37. Hong SS, Lee MS, Park SS, Lee GD (2003) Catal Today 87:99